Journal of the European Ceramic Society 44 (2024) 116700

Contents lists available at ScienceDirect

Journal of the European Ceramic Society

journal homepage: www.elsevier.com/locate/jeurceramsoc

Spark plasma sintering of boron carbide (B_4C): From characterisation to finite element modeling of sintering

Thomas Grippi [a,*], Elisa Torresani [a], Andrii L. Maximenko [a], Eugene A. Olevsky [a,b]

[a] Mechanical Engineering, San Diego State University, San Diego, CA, USA
[b] Nano-Engineering, University of California, La Jolla, San Diego, USA

ARTICLE INFO

Keywords:
Boron carbide
Sintering modeling
Spark plasma sintering
Finite element model

ABSTRACT

Boron carbide (B_4C), known for its unique properties, presents challenges in reaching its full density with sintering process due to low diffusion coefficients. This study explores the application of Spark Plasma Sintering (SPS) to overcome these challenges and enhance the understanding of its impact on pure B_4C ceramics. The study outlines a comprehensive methodology for developing an SPS sintering model. Starting with a summary of conducted studies, powder oxidation analysis, characterization methods, and dilatometry curves processing, the article details the derivation of constitutive parameters based on the Skorohod-Olevsky theory. Isothermal profiles at different temperatures, variation in heating regimes, and a stepwise approach for SPS pressure application form the basis of the derivation methods. A grain growth model is developed for a comprehensive simulation of sintering, incorporating microstructural analysis and parameter derivation. Finally, the article addresses the integration of this mechanical sintering model with thermal and electrical considerations into a finite element method (FEM) software for a holistic SPS modeling. Thermo-electrical considerations, including the Peltier effect, are also computed, providing a well-rounded understanding of the SPS process for B_4C ceramics. This study contributes valuable insights to optimizing the SPS parameters to achieve enhanced densification and microstructure control in B_4C ceramics.

1. Introduction

Boron carbide is a versatile material known for its low density of 2.52 g/cm^3, its exceptional hardness (only surpassed by diamond and cubic boron nitride), remarkable thermal stability, and outstanding ability to absorb neutrons that gives it a wide range of potential applications across various industries such as armor technology and nuclear engineering [1–3]. However, attaining the complete theoretical density of B_4C ceramics poses a challenge due to the low diffusion coefficient, attributed to the robust covalent bond between B and C, and the delay in the densification process by the presence of B_2O_3 on the surface of B_4C.

Pressureless sintering has the capability to produce B_4C ceramics with a relative density up to 90 %. However, this exhibits a considerable amount of remaining pores, which can subsequently diminish the overall performance of the B_4C ceramics [4,5]. It is noteworthy that achieving pressureless sintering for B_4C ceramics requires elevated temperatures near the melting point (~2350°C). Unfortunately, such high temperatures may induce grain coarsening, thereby negatively impacting the final performance of the B_4C ceramics.

In order to lower the sintering temperature of B_4C ceramics, various additives (such as C, Ti, Cr, Ni, Cu, TiB_2, TiC, Al_2O_3, etc.) have been explored to accelerate the densification process [6–10]. However, the inclusion of these sintering additives may introduce additional impurity phases into the end product. Maintaining high purity in B_4C ceramics is crucial for numerous applications, especially in the nuclear field so the ad of dopants is not a solution for all the applications.

The Spark Plasma Sintering (SPS) is a material processing technique that utilizes a combination of high-voltage electric current and uniaxial mechanical pressure to facilitate the densification and consolidation of powder materials [11–14]. Its renowned feature lies in its ability to rapidly increase the density of materials that are traditionally challenging to sinter, like carbides and other high-temperature systems, which cannot achieve high density through conventional sintering methods [15]. The rapid heating rates it can attain enable the mitigation of grain growth, particularly beneficial when sintering nanosized powders and makes it ideal sintering method for the production of structural ceramics such as boron carbide. In addition to boron carbide, researchers have explored the sintering of other carbides using SPS, including tungsten carbide (WC) [16], zirconium carbide (ZrC) [17] and

* Corresponding author.
E-mail address: tgrippi@sdsu.edu (T. Grippi).

https://doi.org/10.1016/j.jeurceramsoc.2024.116700
Received 21 March 2024; Received in revised form 24 June 2024; Accepted 25 June 2024
Available online 6 July 2024

Nomenclatures

ρ	Density	θ	Porosity
ρ_w	Density of water	T	Temperature
W_1	Dry weight	$\dot{\varepsilon}_{eq}$	Equivalent stain rate
W_2	Weight impregnated with oil	σ_{eq}	Stress tensors
W_3	Weight of the impregnated sample in water	ψ	Bulk modulus
D_f	Final density	φ	Shear modulus
h_f	Final height	θ	Porosity
h_t	Height at the specific time t	τ	Stress invariant
D_t	Density at the specific time t	P	Applied pressure
G	Mean grain size	$\dot{\gamma}$	Shear strain rate
n	Creep law stress exponent	$\dot{e}$	Volumetric strain rate
A_0	Deformability pre-exponential factor	P_l	Laplace stress
G	Grain size	$\underline{\sigma}$	External stress tensor
G_0	Initial grain size	$\underline{\dot{\varepsilon}}$	External strain rate tensor
m	Grain growth exponent	k_0	Grain growth pre-exponential factor
Q	Apparent sintering activation energy	Q_G	Grain growth activation energy
		ρ_c	Critical density

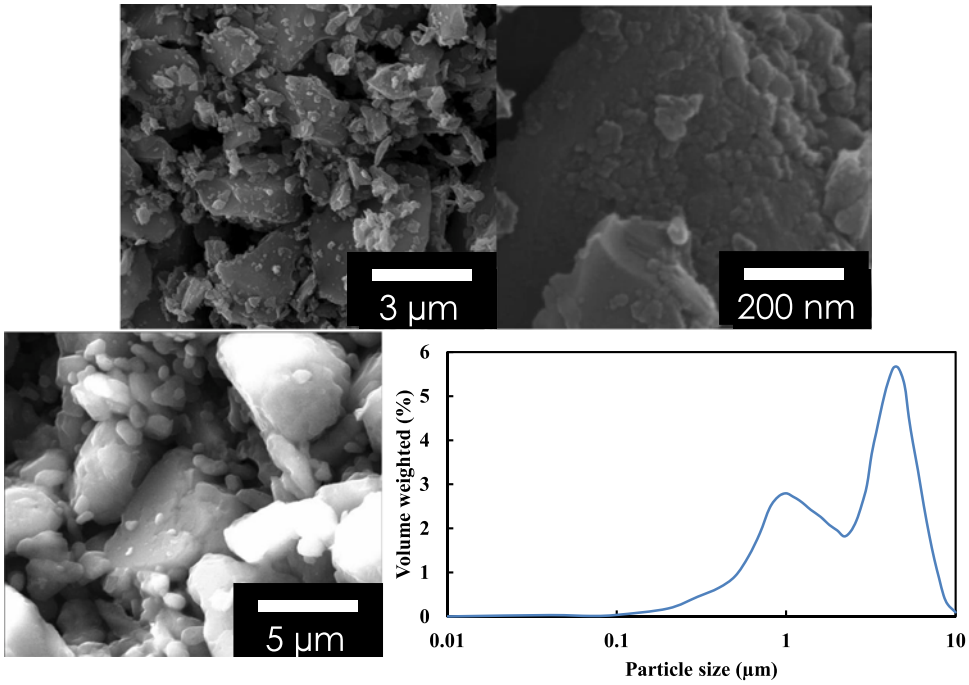

Fig. 1. SEM of the initial powder at magnification x117k (top left) and x160k (top right) and at initial sintering stage before grain growth x7600 (bottom left); bimodal particle size distribution of the powder agglomerates (bottom right).

tantalum carbide (TaC) [18].

While SPS has been extensively employed for the sintering of B_4C ceramics, a majority of studies have focused on a limited set of parameters to understand their impact on ceramic properties. Liu et al. [19], for instance, investigated the effects of varying sintering temperatures on the relative density and microstructure of B_4C ceramics without additives. Notably, they achieved a B_4C ceramic with a density of 98 %, a hardness of 33.5 ± 0.2 GPa, and a toughness of 3.21 ± 0.13 MPa·$m^{1/2}$ at 1850°C with an ideal heating rate of 100 °C/min and an applied pressure of 50 MPa.

Therefore, there is a significant need for a process modeling to understand the influence of various SPS parameters on the densification and final microstructure of B_4C ceramics.

In this study the necessary and sufficient methodology is depicted to develop a comprehensive SPS sintering model. After a brief summary of the conducted studies, powder oxidation analysis, methods of characterization and dilatometry curves processing, the article details the derivation of constitutive parameters based on the Skorohod-Olevsky theory of continuum sintering [20]. Numerous alternative models have been proposed [21], including those by Skorohod-Olevsky [20], Abouaf [22,23], Kraft and Riedel [24], and formulations based on the viscous poisons ratio [25,26]. The derivation methods outlined in this research are held on isothermal profiles at different temperatures, considering variations of the heating regimes and stepwise approach for SPS pressure application [27–30]. For the most comprehensive simulation of sintering, a grain growth model is developed based on microstructural analysis and grain growth model parameters' derivation [11, 31].

Finally, the article addresses the integration in a finite element method (FEM) software of such mechanical sintering model coupled to thermal and electrical considerations for a comprehensive SPS modeling. Thermo-electrical considerations accounting for the Peltier effect are also computed [32].

2. Methods and experiments

2.1. Material processing and characterization

The studied material is a commercial powder of boron carbide (Cerion Nanomaterials, Rochester, NY). Size and shape of the powder are analyzed from the Scanning Electron Microscopy images in Fig. 1 left and right (FEI Quanta 450 FEG). It is composed of non-spherical particles with an average diameter of 25 nm (Fig. 1 right) agglomerated in a bimodal distribution of 0.6 μm to 0.8 μm and 2 μm to 5 μm of broad agglomerates Fig. 1 top left). These observations on the bi-modal distribution of the agglomerates are confirmed by the particle size distribution analysis performed on Anton Paar PSA 1090 in Fig. 1 (bottom right). Identified distribution parameters are D_{10}= 0.54 μm, D_{50} 2.48 μm and D_{90}=5.48 μm with a mean size of 2.87 μm. Particle size distribution has also been measured from a compacted sample after an experiment performed at low temperature before initial sintering stage, confirming the initial mean grain size and bimodal distribution Fig. 1.

The initial powder density has been measured by pycnometry via a helium pycnometer Anton Paar Ultrapyc 5000. The measured initial density of 2550 kg.m^{-3} is close from the boron carbide theoretical one 2520 kg.m^{-3}[1].

2.2. Methods for samples preparation and powder washing

For all the sintering experiments conducted on the SPS, 2 g of pure B_4C powder have been prepared in a 15 mm diameter graphite die. Contacts between the die, the punches and the powder were made by graphite foil. All the experiments performed at PTL were using an SPS system SPSS DR.SINTER Fuji Electronics model 515. Temperature is regulated by an embedded PID via infra-red pyrometry with Chino IR-AHS.

An additional comparative study to determine the importance of the powder oxidation [33] has been held between original powder batch and washed powder batch. In this precise case, 5 g of powder has been stirred in 10 ml of methanol, then dried in vacuum at 80°C for 2 hours. In this process, boric acid undergoes conversion into trimethyl borate, which subsequently evaporates as an azeotrope with methanol [34]. The quantification of powder oxidation incidence during the initial sintering stage at low temperatures has been added to the supplementary materials section.

After sintering process, dense samples were measured by a 3 weighing Archimedes method [35].

$$\rho = \frac{W_1 \rho_w}{W_2 - W_3} \quad (1)$$

With ρ [g cm^{-3}] the sample density, ρ_w [g cm^{-3}] the density of water, W_1 [g] the dry weight, W_2 [g] the weight impregnated with oil and W_3 [g] the weight of the impregnated sample in water.

2.3. Experimental results

Dilatometry data issued from the SPS are vertical displacement as function of time and temperature. The density evolution during the temperature profile in a die compacting can be calculated from the expression:

$$\rho_t = \frac{\rho_f}{h_t} h_f \quad (2)$$

With ρ_f [g cm^{-3}] the final density, h_f the final height, h_t [cm] and ρ_t [g cm^{-3}] the height and the density at the specific time t [s], respectively.

Table 1
Specimen measurements post-sintering and their corresponding thermal profiles.

Temperature Profile	Final height (mm)	Final radius (mm)	Weight (g)	Bulk density	Relative density
1500°C for 15 min, 60 MPa, 50 °C/min	7.31	7.50	2.14	1.70	**67.5 %**
1500°C for 15 min, 80 MPa, 50° C/min	6.62	7.50	2.26	1.90	**75.4 %**
1600°C for 15 min, 60 MPa, 50° C/min	8.68	7.50	2.70	1.76	**69.8 %**
1800°C for 15 min, 60 MPa, 50° C/min	5.50	7.50	1.96	2.06	**81.7 %**
1800°C for 15 min, 60 MPa, 100° C/min	4.49	7.50	1.92	2.45	**97.2 %**
1800°C for 15 min, 60 MPa, 25° C/min	5.45	7.50	2.04	2.16	**85.7 %**
1800°C for 15 min, 60 MPa, 75° C/min	4.57	7.50	1.89	2.42	**96.0 %**
1800°C for 0 min, 60 MPa, 75° C/min	5.23	7.50	1.97	2.13	**84.7 %**
1800°C for 8 min, 60 MPa, 75° C/min	4.54	7.50	1.91	2.38	**94.5 %**
1800°C for 15 min, Pressure variations, 50 °C/min	5.55	7.50	1.93	2.42	**96.0 %**
1500°C 60 Mpa 50 °C/min (washed with methanol)	7.4	7.50	2.12	2.26	**89.7 %**
1800°C for 15 min, 60 MPa 100 °C/min	4.42	7.50	1.86	2.39	**94.9 %**
1800°C then 1700°C for 15 min, 60 MPa	5.76	7.50	1.95	2.07	**82.2 %**

Measurements on samples from the different conducted studies have been gathered in the Table 1. Details on preliminary studies at 1500°C and 1600°C mentioned in the Table 1 are in the supplementary material section of the article. The final height and density values are taken as reference for the evaluation of the relative density as function of the time with Eq. (2).

2.4. Experiments

2.4.1. Variations on the heating rates

A comprehensive investigation involving multiple sintering experiments has been conducted. These experiments used temperature profiles with different heating rates, reaching a maximum temperature of 1800°C and a die compaction pressure of 60 MPa. The results obtained from these experiments, with heating rates ranging from 25 °C/min to 100 °C/min, are presented in Fig. 2. Data analysis reveals nearly complete densification at heating rates of 75 °C/min and 100 °C/min, achieving final relative densities of 96.0 % and 97.2 %, respectively. Examining Fig. 2 and Table 1, it is evident that the minimum final density is observed for the run at 50 °C/min, reaching 81.3 % relative density. The notable aspect is the acceptable densification achieved, nearly attaining full density under specific conditions without

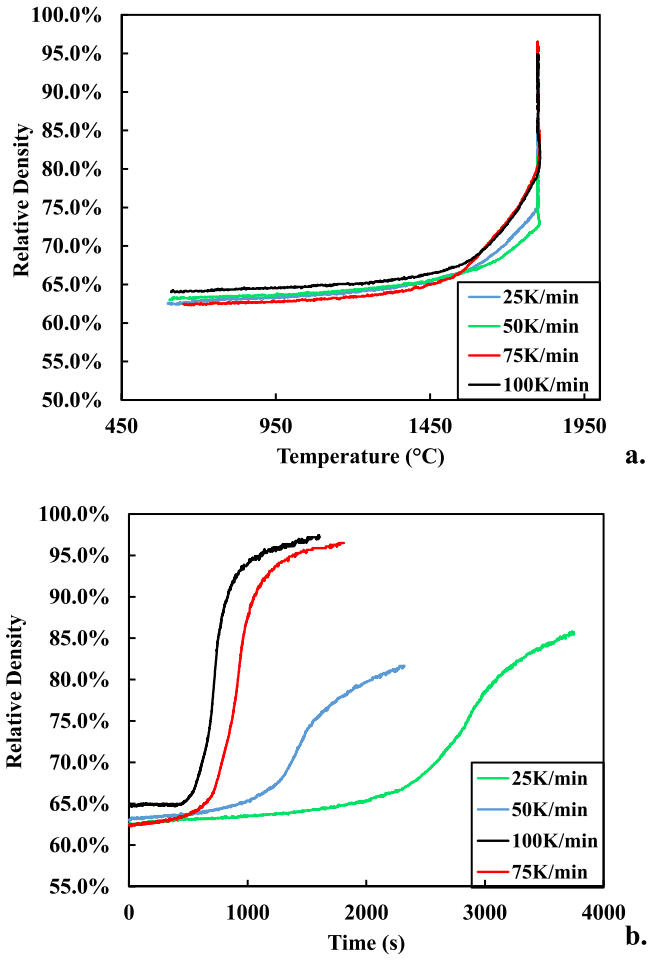

Fig. 2. Relative density as a function of temperature (a.) and time (b.) for thermal profile at 1800°C and heating rates ranging from 25 °C/min to 100 °C/min.

encountering thermal runaway or local melting.

In the literature [15], it is noted that a heating rate below 85 °C/min results in abnormal grains in the lower part of SPS-sintered samples, thereby impacting final densification. Similar to our findings, the sub-optimal densification configuration in our study occurs at 50 °C/min, while 75 °C/min and 100 °C/min exhibit a more favorable densification response.

The slowest heating regime of the study, 25 °C/min, shows a higher densification than the one during the experiment with a 50 °C/min heating regime. For this particular case, a parallel could be made with this SPS study to the sintering of alumina by Demuynck *et al.* [36] where it is stated that SPS's PID is not optimal for a regulation at low heating rate. A thermal profile with a heating rate below 50 °C/min with this technique could thus explain this experimental result. Results from simple preliminary sintering experiments displayed almost fully dense and refined microstructure from without any problematics of melting and thermal runaway. Conducting an SEM microstructural analysis of the sample should provide a quantitative assessment of the significance of the grain growth phenomenon and the grain size distribution in the sample. On the other hand, based on the accurate and almost fully dense samples data, the derivation of the constitutive parameters for a sintering simulation is now possible.

3. Microstructural analysis

Microstructural analysis has focused on the sample from the experiment following the temperature profile of 75 °C/min, 15 min at 1800°C and with 60 MPa uniaxial pressure. The specimen has been sliced and polished before SEM observation (FEI Quanta 450 FEG). Prior to revealing the microstructure with backscattered electron detector (Fig. 3 left) an electro-etching has been performed with KOH solution under a 0.2 A current for 20 s.

Fig. 3 presents dense homogeneous granular microstructure with a few pores (left) and the fracture profile with similar grain size distribution (right).

From micrographs above the grain size has been identified via the linear intercepts method [31,37].

$$G = \frac{X * 1.56}{N} \tag{3}$$

Mean grain size G [m] is calculated from the ratio between the number of the grain boundaries X within a line of length N [m] and multiplied by a standard stereological factor of 1.56. Grain size distribution in the sample does not take into account the abnormal grain sizes with a mean grain diameter of 2.98 μm close to the top surface (Area α, Fig. 4) and 2.8 μm close to the bottom surface of the sample (Area β, Fig. 4). Accordingly, based on the linear intercept method, the general mean final grain size is 2.91 μm.

Additional two interrupted sintering experiments have been performed to quantify the microstructure evolution, as shown in Fig. 4. The quenches follow similar temperature and pressure profiles, with one experiment including an 8-minute temperature hold after reaching 1800°C and the other without a temperature hold. The same characterization method revealed an average grain size of 1.6 μm for the experiment without temperature without significant variation from the bottom to the top of the sample. The second specimen showed an

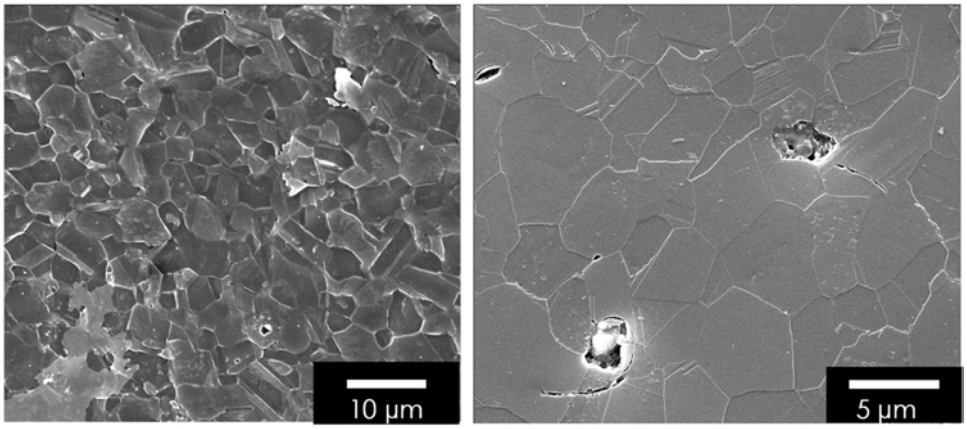

Fig. 3. Secondary electron microscopy micrograph at magnification x10k (left) back scattered electron microscopy micrograph at magnification x29k (right).

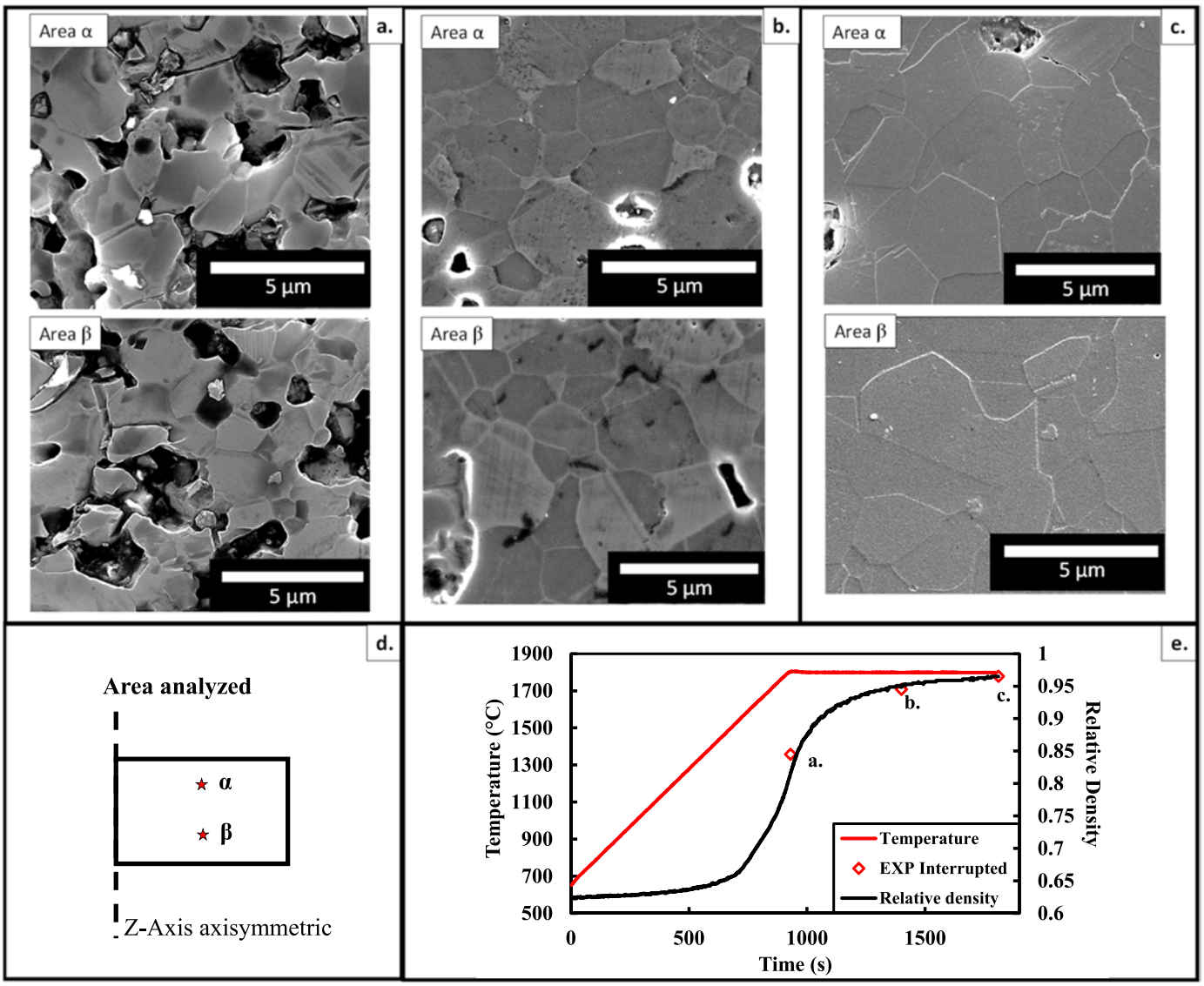

Fig. 4. Microstructure of specimen interrupted at 0 min, (a.), 8 min (b.) and 15 min (c.) of the temperature holding. Schematic of areas analyzed for microstructure characterisation (d.). Relative density and microstructural evolution for the temperature profile 75 °C/min, 1800°C for 15 min.

average grain size of 2.47 µm, with a mean grain diameter of 2.58 µm close to the top surface (Area α) and 2.36 µm close to the bottom surface (Area β) of the sample.

4. Data processing and modelling

4.1. Model description

From the continuum theory of sintering [20], one can consider the studied samples to have a creep underlying dense phase behavior. The equivalent stress and strain rate equations obey Norton creep law:

$$\dot{\varepsilon}_{eq} = A(T,G){\sigma_{eq}}^{n} = A_0\left(\frac{G_0}{G}\right)^{m}\frac{\exp(\frac{-Q}{RT})}{T}{\sigma_{eq}}^{n} \tag{4}$$

with n being the creep law stress exponent, A_0 [K·s^{-1}·Pa^{-n}] the deformability pre-exponential factor, G [m] the grain size, G_0 [m] the initial grain size, m the grain growth exponent, Q [J mol^{-1}] the apparent sintering activation energy and T [K] the absolute temperature.

Equivalent stain rate and stress tensors are defined as:

$$\dot{\varepsilon}_{eq} = \frac{1}{\sqrt{1-\theta}}\sqrt{\varphi\dot{\gamma}^2 + \psi\dot{e}^2} \tag{5}$$

$$\sigma_{eq} = \frac{\sqrt{\frac{\tau^2}{\varphi} + \frac{(P-P_i)^2}{\psi}}}{\sqrt{1-\theta}} \tag{6}$$

where φ and ψ are respectively the normalized shear and bulk moduli, functions of the porosity θ. Terms τ [MPa], P [MPa], $\dot{\gamma}$ [s^{-1}] and $\dot{e}$ [s^{-1}] are the stress and strain rate invariants defined below.

$$\tau = \frac{\sqrt{\left(\sigma_x-\sigma_y\right)^2 + \left(\sigma_y-\sigma_z\right)^2 + \left(\sigma_z-\sigma_x\right)^2 + 6\left(\sigma_{xy}^2+\sigma_{yz}^2+\sigma_{xz}^2\right)}}{\sqrt{3}} \tag{7}$$

$$P = \frac{\sigma_x+\sigma_y+\sigma_z}{3} = \frac{I_1}{3} \tag{8}$$

$$\dot{\gamma} = \sqrt{2\left(\dot{\varepsilon}_{xy}^2+\dot{\varepsilon}_{xz}^2+\dot{\varepsilon}_{yz}^2\right) + \frac{2}{3}\left(\dot{\varepsilon}_x^2+\dot{\varepsilon}_y^2+\dot{\varepsilon}_z^2\right) - \frac{2}{3}\left(\dot{\varepsilon}_x\dot{\varepsilon}_y + \dot{\varepsilon}_x\dot{\varepsilon}_z + \dot{\varepsilon}_y\dot{\varepsilon}_z\right)} \tag{9}$$

$$\dot{e} = \dot{\varepsilon}_x + \dot{\varepsilon}_y + \dot{\varepsilon}_z \tag{10}$$

The term P_l [MPa] is the Laplace stress originated from particle capillarity forces. The latter can be defined by the particle radius and the porosity from Skorohod-Olevsky theory [20,38].

$$Pl = \frac{3\alpha}{r}(1-\theta)^2 \tag{11}$$

In the present case of SPS, the capillarity forces can be neglected compared to the applied stress ($P_l \ll \sigma_z$).

The mass conservation law is used to link the rate of porosity elimination with volume change rate.

$$\frac{\dot{\theta}}{(1-\theta)} = \dot{e} \tag{12}$$

Finally, the general sintering behavior of a continuum can be defined as:

$$\underline{\sigma} = \frac{\sigma_{eq}}{\dot{\varepsilon}_{eq}}\left(\varphi\underline{\dot{\varepsilon}} + \left(\psi - \frac{1}{3}\varphi\right)\dot{e}\,\underline{\mathbb{i}}\right) + P_l\,\underline{\mathbb{i}} \tag{13}$$

4.2. Specific case for SPS

Spark Plasma Sintering can be assimilated to a high temperature die pressing test (along the z-axis). The external strain rate tensor can be reduced to:

$$\underline{\dot{\varepsilon}} \equiv \begin{pmatrix} 0 & 0 & 0 \\ 0 & 0 & 0 \\ 0 & 0 & \dot{\varepsilon}_z \end{pmatrix} \tag{14}$$

The lateral friction is neglected via the use of graphite foil interface. Based on Eq. (12), we can simplify.

$$\dot{e} = \dot{\varepsilon}_z, \dot{\gamma} = |\dot{\varepsilon}_z|\sqrt{\frac{2}{3}}, \dot{\varepsilon}_{eq} = |\dot{\varepsilon}_z|\sqrt{\frac{\psi + \frac{2}{3}\varphi}{1-\theta}} \tag{15}$$

With combination of Eqs. (4), (13), (14) and (15) the stress toward z direction, σ_z term, is:

$$\sigma_z = \frac{\dot{\varepsilon}_{eq}^{\frac{1}{n}} - 1}{A(T,G)^{\frac{1}{n}}}\left(\varphi\dot{\varepsilon}_z + \left(\psi - \frac{1}{3}\varphi\right)\dot{\varepsilon}_z\right) \tag{16}$$

The analytical SPS equation is then:

$$|\dot{\varepsilon}_z| = A_0\left(\frac{G_0}{G}\right)^m \frac{\exp\left(\frac{-Q}{RT}\right)}{T}\left(\psi + \frac{2}{3}\varphi\right)^{\frac{-n-1}{2}}(1-\theta)^{\frac{1-n}{2}}|\sigma_z|^n \tag{17}$$

With ψ and φ the normalized shear and bulk viscosity moduli expressed as:

$$\psi = \frac{2}{3}\frac{(1-\theta)^3}{\theta} \text{and} \psi = (1-\theta)^2 \tag{18}$$

From the Eq. (17), the constitutive parameters to be determined are then the creep law stress exponent n, the activation energy Q and the pre-exponential factor A_0.

4.3. Derivation of the creep law stress exponent: n

In this part, the stress exponent n is identified. The method, based on analytic equations detailed above, follows a similar procedure than the one detailed in Maniere *et al.*[27] and Li *et al.* [28] publications. The technique involves implementing specific "pressure jumps" while maintaining a constant temperature. In this application, the method is employed to determine the exponent "n" by analyzing the change in sintering shrinkage rate before and after the pressure "jump." It is crucial for the abrupt pressure change to be sufficiently rapid to prevent significant fluctuations in relative density.

From analytical Eq. 16 we can isolate n term:

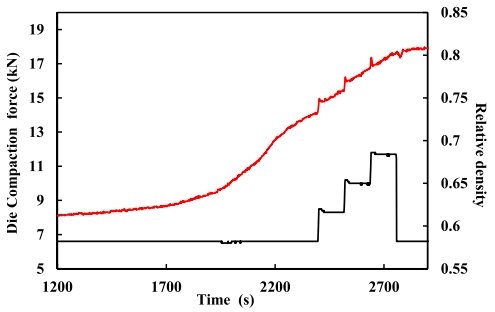

Fig. 5. Measured die compaction force and relative density of the studied specimen as a function of time with a temperature profile up to 1800°C with a heating rate of 50 °C/min.

$$|\dot{\varepsilon}_z| = A\frac{\sqrt{1-\theta}}{\sqrt{\psi + \frac{2}{3}\varphi}}\left(\frac{\sigma_z}{\sqrt{1-\theta}\sqrt{\psi + \frac{2}{3}\varphi}}\right)^n \tag{19}$$

If the pressure jumps of the stepwise approach result in no changes in porosity, the ratio of the strain rates before and after the pressure variation simplifies all terms dependent on porosity. Consequently, the formulation (19) is thus simplified to:

$$n = \frac{\ln\left(\frac{\dot{\varepsilon}_1}{\dot{\varepsilon}_2}\right)}{\ln\left(\frac{\sigma_1}{\sigma_2}\right)} \tag{20}$$

On the other hand, if the pressure transition implies a porosity evolution which is not negligible, the strain rate ratio can be expressed:

$$\frac{\dot{\varepsilon}_1}{\dot{\varepsilon}_2} = \frac{\sqrt{1-\theta_1}\sqrt{\psi_2 + \frac{2}{3}\varphi_2}}{\sqrt{1-\theta_2}\sqrt{\psi_1 + \frac{2}{3}\varphi_1}}\left(\frac{\sigma_1\sqrt{1-\theta_2}\sqrt{\psi_2 + \frac{2}{3}\varphi_2}}{\sigma_2\sqrt{1-\theta_1}\sqrt{\psi_1 + \frac{2}{3}\varphi_1}}\right)^n \tag{21}$$

By isolating the n term and taking the logarithm, we thus have:

$$n = \frac{\ln\left(\frac{\dot{\varepsilon}_1}{\dot{\varepsilon}_2}\frac{\sqrt{1-\theta_2}\sqrt{\psi_1 + \frac{2}{3}\varphi_1}}{\sqrt{1-\theta_1}\sqrt{\psi_2 + \frac{2}{3}\varphi_2}}\right)}{\ln\left(\frac{\sigma_1}{\sigma_2}\frac{\sqrt{1-\theta_1}\sqrt{\psi_2 + \frac{2}{3}\varphi_2}}{\sqrt{1-\theta_2}\sqrt{\psi_1 + \frac{2}{3}\varphi_1}}\right)} \tag{22}$$

Skorohod theoretical moduli are used in this study (Eq. 18), hence the expression (22) can be reformulated as:

$$n = \frac{\ln\left(\frac{|\dot{\varepsilon}_1|}{|\dot{\varepsilon}_2|}\sqrt{\frac{(1-\theta_1)\theta_2}{(1-\theta_2)\theta_1}}\right)}{\ln\left(\frac{\sigma_1}{\sigma_2}\sqrt{\frac{(1-\theta_2)\theta_1}{(1-\theta_1)\theta_2}}\,\frac{(1-\theta_2)}{(1-\theta_1)}\right)} \tag{23}$$

In the experimental study, three pressure jumps of 10 MPa each were executed, transitioning from 37 MPa to 67 MPa. Each holding step lasted 2 minutes with a stepwise pressure application every 10 seconds. This was carried out during a temperature hold at 1800°C with a heating rate of 50 °C/min. Based on the experimental data (as depicted in Fig. 5) and Eq. (23), the parameter "n" was identified as n=1.89. This value closely aligns with n=2, as reported in Diatta et al. analogous work on the characterization and modeling of spark plasma sintering of boron carbide [32]. Consistent with these findings, [39] literature also associates the exponent "n" with a value of 2.

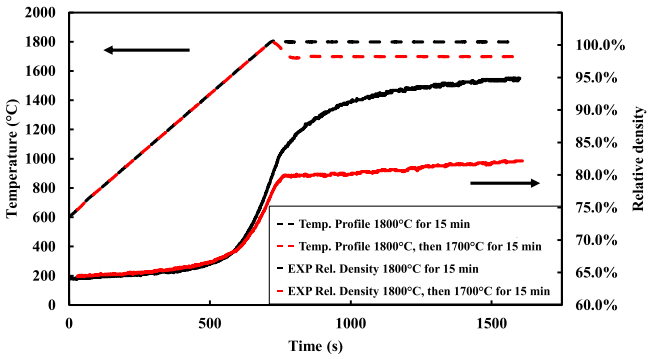

Fig. 6. Thermal profiles and relative density as function of the time for experiments conducted at 1800°C for 15 min (in black) and at 1800°C then 1700°C for 15 min (in red).

4.4. Derivation of the activation energy: Q

Initially, the variation in the heating rate, presented above, was intended to serve as data for identifying the apparent sintering activation energy using methods such as the master sintering curve (MSC) [30] or kinetic fields [40–42]. However, in our case, processing data within a narrow experimental non-isothermal zone could potentially yield biased results. In light of this, we opted for an isothermal method in this study, and its application for deriving the activation energy is discussed in the following section.

As reported in Maniere *et al.* work [22], the value of the creep law activation energy Q can be determined via tests at different holding temperatures. From the analytical expression (17) and (12) we can formulate:

$$\left|\frac{\dot{\theta}}{(1-\theta)}\right| = A_0\left(\frac{G_0}{G}\right)^m \frac{\exp\left(\frac{-Q}{RT}\right)}{T}\left(\psi+\frac{2}{3}\varphi\right)^{\frac{-n-1}{2}}(1-\theta)^{\frac{1-n}{2}}|\sigma_z|^n \tag{24}$$

For two SPS compaction tests at the same applied stress σ_z and the same porosity θ, and for different temperature holding:

$$\left|\frac{\dot{\theta}_1}{\dot{\theta}_2}\right|\frac{T_1}{T_2} = \frac{\exp\left(\frac{-Q}{RT_1}\right)}{\exp\left(\frac{-Q}{RT_2}\right)} = \exp\left(\frac{Q}{R}\left(\frac{1}{T_2}-\frac{1}{T_1}\right)\right) \tag{25}$$

Isolating the apparent sintering activation energy *Q*:

$$Q = \frac{R\ln\left(\frac{\dot{\theta}_1}{\dot{\theta}_2}\frac{T_1}{T_2}\right)}{\frac{1}{T_2}-\frac{1}{T_1}} \tag{26}$$

In the experimental study, two SPS experiments with similar thermal profiles were conducted, employing a 60 MPa pressure and a heating rate of 100 °C/min. The first experiment was carried out at 1800°C for 15 minutes (depicted in black in Fig. 6), while the second experiment reached 1700°C for 15 minutes following a peak temperature of 1800°C, illustrated in red in Fig. 6 below. Subsequently, using the Eq. (26) and experimental data, the activation energy (*Q*) was derived for a relative density ranging from 79 % to 82 %, resulting in an identified value of 345 kJ/mol. This value closely aligns with the findings of Diatta et al., who reported values of 292 kJ/mol and 385 kJ/mol [43].

4.5. Grain growth modeling

In this task, the modeling of grain growth has been conducted using the experimental data presented in Section 4, with a mean initial grain size of 1 μm and a final average grain size of 2.9 μm. The grain growth has been modeled using the expression (27), which describes the grain growth rate as a function of relative density and grain size [11].

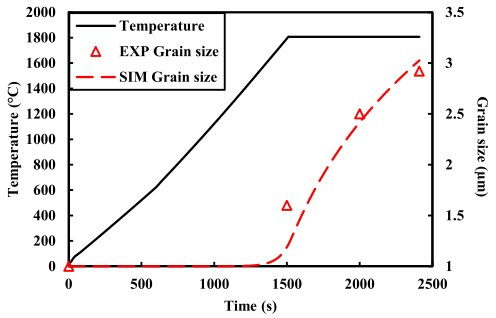

Fig. 7. Experimental average grain size, simulated mean grain size evolution as the function of the time following a temperature profile up to 1800°C for 15 min with a heating regime of 75 K/min.

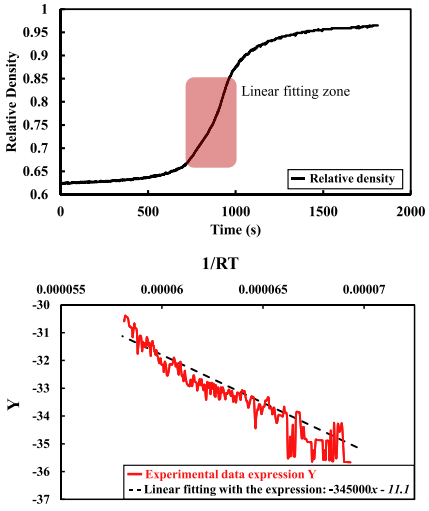

Fig. 8. Densification data from sintering experiment conducted with 75 °C/min heating rate up to 1800°C (above) and linear fitting to derive A_0 from the identified parameter Q from the same data set (below).

$$\frac{dG}{dt} = \frac{k_0}{3G^2}\left(\frac{1-\rho_c}{2-\rho_c-\rho}\right)^{\frac{3}{2}}\exp\left(\frac{-Q_G}{RT}\right) \tag{27}$$

Using Eq. (25) and sintering data, the following parameters were fitted: the pre-exponential factor k_0 is set to 5E-14 $m^3\,s^{-1}$, and the grain growth activation energy Q_G is determined to be 240 kJ/mol and a critical density parameter representing the relative density from which the grain growth starts ρ_c= 0.9 as can be observed below on Fig. 7. The latter figure also gather grain size evolution from conducted quenches experiments.

4.6. Fitting with linearization for the derivation of A_0

From the mass conservation law (10), the Eq. (15) can be rearranged and linearized with a logarithm form to isolate *Q* and A_0 as below[44]:

$$Y = \ln\left(T|\dot{\theta}|\left(\frac{G_0}{G}\right)^m\left(\psi+\frac{2}{3}\varphi\right)^{\frac{n+1}{2}}(1-\theta)^{\frac{n-3}{2}}|\sigma_z|^{-n}\right) = \ln(A_0) - \frac{Q}{RT} \tag{28}$$

For the purpose of this study, the reference profile is 1800°C for 15 min, uniaxial pressure of 60 MPa, 75 °C/min where the final relative density has reached 96 %. In this case the regression is focused in a zone with limited grain growth, below 85 %RD (see Fig. 8) so the term A is simplified to its formulation:

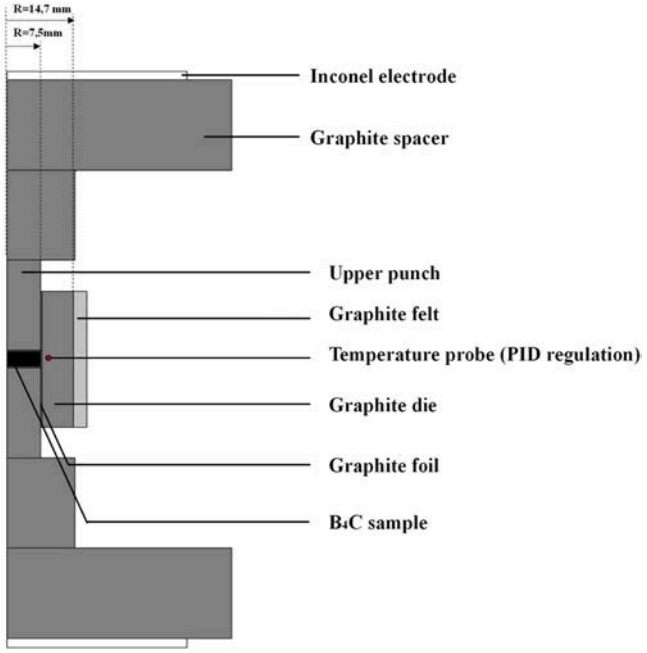

Fig. 9. Axisymmetric geometry for FEM model of SPS.

Table 2
Properties of inconel, graphite, and graphite felt.

Properties	Inconel	Graphite	Graphite felt
Electrical conductivity ($S{\cdot}m^{-1}$)	$1/(1.6\times 10^{-10}\times T+9.82\times 10^{-7})$	$1/(5.81\times 10^{-16}\times T^3+1.29\times 10^{-12}\times T^2-9.17\times 10^{-9}\times T+1.84\times 10^{-5})$	333
Thermal conductivity ($W{\cdot}m^{-1}{\cdot}K^{-1}$)	$-1.57\times 10^{-2}\times T+10.09$	$-6.13\times 10^{-9}\times T^3+3.74\times 10^{-5}\times T^2-8.55\times 10^{-2}\times T+100.05$	For T<1273 K $2.00\times 10{-}7\times T^2-1.90\times 10^{-4}\times T+0.14$ For T > 1273 0.217
Heat capacity ($J{\cdot}kg^{-1}{\cdot}K^{-1}$)	$0.250\times T+344$	$-9.6\times 10^{-4}\times T^2+2.72\times T{-}34.27$	For T<1673 K $0.69\times T+507.53$ For T > 1673 K 1675
Density ($kg{\cdot}m^{-3}$)	8430	1860	88
Young's modulus (GPa)	400	180	-
Poisson's ratio (-)	0.29	0.262	-
Seebeck coefficient ($V{\cdot}K^{-1}$)	-	$2.28\times 10^{-11}\times T^2-4.27\times 10^{-8}\times T+1.16\times 10^{-5}$	-
Emissivity (-)	0.67	0.8	0.99

$$A(T)=A_0\frac{\exp\left(\frac{-Q}{RT}\right)}{T} \tag{29}$$

The value of Q is fixed for a linear fitting from the identified value detailed in the previous part.

The identified value for the deformability pre-exponential factor is A_0 =1.5112E-5 ($K{\cdot}s^{-1}{\cdot}Pa^{-n}$)

5. Results and discussion

In this section, the mechanical model is integrated into the COMSOL Multiphysics™, a commercial finite element software. This software facilitates the coupling of various physical aspects of the SPS furnace with the mechanical sintering model, allowing for a comprehensive electrical-thermal-mechanical simulation, including the incorporation of thermoelectrical effects. For the study, the sintering configuration is computed as a 2D axisymmetric model, as illustrated in the geometry shown in Fig. 9.

Table 3
Properties of boron carbide powder as a function of the relative density.

Properties	Boron carbide
Electrical conductivity ($S{\cdot}m^{-1}$)	$\left(1-\frac{3}{2}(1-\rho)\right)/(7.67\times 10^{-13}\times T^4-2.74\times 10^{-9}\times T^3+3.58\times 10^{-6}\times T^2-2.03\times 10^{-3}\times T+0.45)$
Thermal conductivity ($W{\cdot}m^{-1}{\cdot}K^{-1}$)	$\left(1-\frac{3}{2}(1-\rho)\right)\cdot(4.87\times 10^{-6}\times T^2-1.91\times 10^{-2}\times T+32.24)$
Heat capacity ($J{\cdot}kg^{-1}{\cdot}K^{-1}$)	$\rho\cdot(8.22\times 10{-}14\times T^5-8.79\times 10^{-10}\times T^4+3.57\times 10^{-6}\times T^3-6.89\times 10^{-3}\times T^2+6.67\times T{-}463.60)$
Young's modulus (GPa)	$(-3.88\times 10^3\times T^2-5.12\times 10^6\times T+4.51\times 10^{11})\cdot\left(\frac{\rho}{1+2.13(1-\rho)}\right)$
Poisson's ratio (-)	0.18
Seebeck coefficient ($V{\cdot}K^{-1}$)	$1.32\times 10^{-4}\times \ln(T)-7.67\times 10^{-4}$

5.1. SPS Model implementations

The implemented SPS model can be depicted as a composition of 6 main components, the flow of electric current, the induced Joule heating, the surface-to-surface radiation, the thermoelectric effects, the densification and the grain growth. The 4 first are solved for both the SPS tooling and the specimen while the 2 last ones are solved for the boron carbide specimen only. Implementation of these components is widely depicted in literature [11,32,45–47].

Thermal, mechanical and electrical properties of the materials used for the simulation are gathered in Tables 2 and 3. Parameters for Inconel, graphite and graphite felt are issued from literature [32,45,48] and properties for boron carbide from[1,32,49]. Analogously to the SPS simulation of boron carbide from Diatta et al.[32], electrical contact resistance are issued from the work of Wei *et al.* [50] and thermal contact resistance on its side are issued from the work of Maniere *et al.*[46].

Initial temperature for the whole tooling is assumed to be 20°C, at this state electric current density in the whole SPS tooling is set to zero.

For the mechanical model outlined in the preceding section, the initial state and boundary conditions are as follows:

- The initial displacement is uniformly set to zero throughout the entire tooling.
- Uniaxial pressure is applied to the upper graphite punch, enabling its vertical displacement.
- The lower punch is fixed within the model and remains without vertical displacement.
- The remaining boundaries are designated as free.

Electrical boundary conditions are: ground is fixed on lower electrode and its potential equals zero. The current is applied to the upper electrode and the current is regulated via a PID controller embedded [47] with the following the expression:

$$I(t)=Kp\cdot e(t)+K_I\int_0^t e(\tau)d\tau+K_D\frac{de(t)}{dt} \tag{30}$$

Most suitable parameters for this PID controlling are K_P=1500, K_I=100 and K_D=10

The distinctive feature of the presented model for the spark plasma sintering of boron carbide powder is its integration with the thermo-electrical model, as discussed in the publication by Diatta et al. [32]. In this literature, a notable thermal gradient was observed in the B_4C sample, resulting in heterogeneity between the top and bottom surfaces. The explanation for the cooling of the bottom junction and heating of the top one lies in the fact that boron nitride is a p-type conductor, while

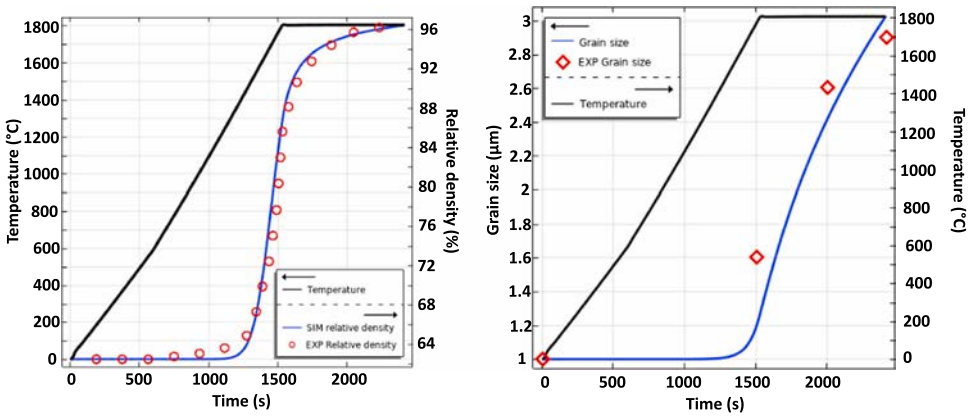

Fig. 10. Thermal profile, experimental data and simulated mean relative density evolution as a function of the time (left). Thermal profile and mean grain size as a function of the time (right).

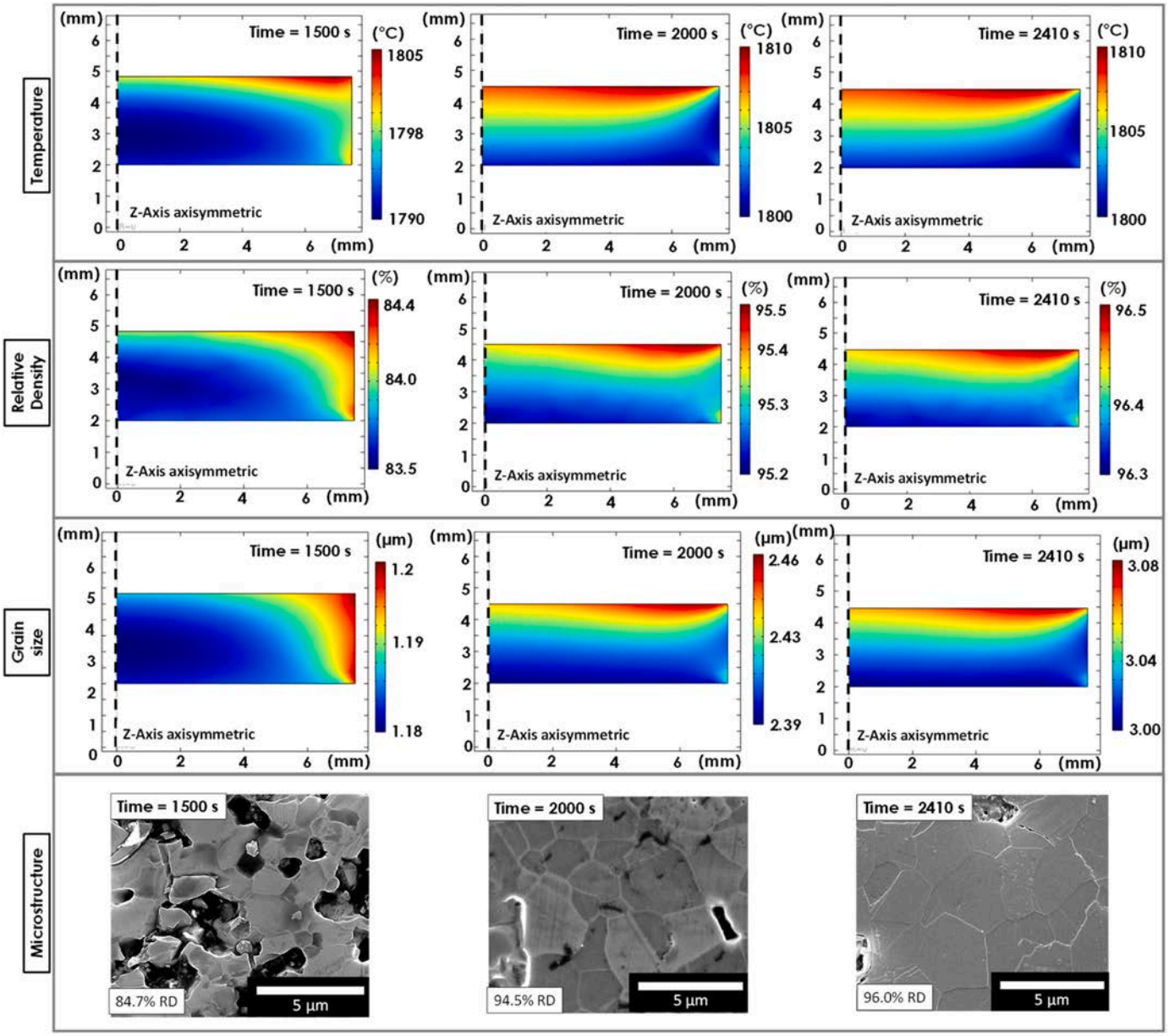

Fig. 11. Temperature, Relative density and grain size distributions during the temperature dwelling at 1800°C and microstructure images and relative density corresponding to time steps 1500 s, 2000s (microstructure displayed analyzed in area β) and 2410 s (microstructure displayed analyzed in area α).

graphite punches are n-type conductors. This phenomenon can be explained by the generation of electron-hole pairs at the bottom and hole recombination at the top of the sample. The Peltier effect is thus non-negligible and needs to be incorporated into our Finite Element Model (FEM).

5.2. Simulation results

The simulated evolution of the mean relative density, when compared to the experimental data, demonstrates a strong correspondence, as depicted in Fig. 10. The presented model, incorporating derived parameters, accurately predicts the densification of the examined specimen.

In Fig. 11, a more detailed depiction of the density distribution during the temperature dwelling at 1800°C is provided for specific time points: t=1500 s (beginning of the holding), t=2000s, and t=2410 s (final sintering time). The density mapping reveals higher densification than the mean value at the top part of the sample and lower densification at the bottom part. Concurrently, the visualization of grain growth at the same time steps in Fig. 11 indicates a similar distribution: thinner grains at the bottom of the sample compared to the top, with a narrow grain size gradient. By comparison with experimental data, the simulated sample show similar relative density at the same time step. The simulated average grain size evolution and its distribution through the thickness of the sample also follows the experimental data. As quantified in the characterization part, at the time step 1500 s the average grain size is of 1.6 μm for the experiment conducted without temperature holding, with no significant size variation from the bottom to the top of the sample. This value is slightly underestimated by the model but could be explained by the experimental precision of the quenching. The simulation result at the timestep at 2000s concords with experimental data conducted with 8 min holding exhibited an average grain size of 2.47 μm. The simulation also demonstrates here its ability to predict the characterized grain growth span as can be observed for the time step at 2000s and the final result at 2410 s of simulation. The grain growth appears to be contained, with a simulated 150 % mean grain growth at the final stage (Fig. 11).

In this study, a significant thermal gradient (≈10°C) is observed in the simulated B4C sample, leading to heterogeneity between the top and bottom surfaces. The cooling of the bottom junction and heating of the top junction can be attributed to the distinct conductive properties of the materials involved: boron nitride acts as a p-type conductor, while graphite punches serve as n-type conductors. This results in the generation of electron-hole pairs at the bottom of the sample and hole recombination at the top [32].

In the present case, the effect is non-negligible, with a 10°C difference during the holding period and up to 15°C at the end of the heating regime at a timestep of 1500 s (Fig. 11) between the top and bottom sections of the sample. Compared to the cited literature [32], the thermoelectric effect observed here seems to be of lower importance. However, experiments and simulations were performed with samples of approximately 2.5 times smaller height, resulting in less pronounced cooling. Therefore, this simulation exhibits relatively lower thermal, density, and microstructural gradients.

6. Conclusion

This article reports details of spark plasma sintering of a boron carbide powder, from powder characterizations to the development of a comprehensive finite element simulation of the powder sintering via SPS. Low microstructural coarsening is also being observed that looks auspicious for future mechanical analysis. The powder has been sintered at up to 1800°C with heating rate ranging from 25 °C/min to 100 °C/min allowing almost full densification for the most favorable cases (97.5 % and 96.0 % relative density for 100°C /min and 75 °C/min).

The description of the methods used for the derivation of constitutive parameters from Skorohod-Olevsky theory of continuum sintering based on the experimental data processing has been at the center of this study. The identification of parameters such as apparent sintering activation energy (345 $kJ \cdot mol^{-1}$), creep law stress exponent(n=1.89) and pre-exponential factor has been discussed.

Finally, the conducted work included the porting of the developed model to a Multiphysics FEM commercial software, COMSOL™, enabling the coupling of thermal, electrical and mechanical physics for an exhaustive simulation of boron carbide spark plasma sintering. It has exhibited a predictive modeling with details on density and grain size distributions linked to temperature gradients in the powder specimen.

CRediT authorship contribution statement

Andrii L. Maximenko: Writing – review & editing, Methodology, Conceptualization. **Thomas Grippi:** Writing – review & editing, Writing – original draft, Software, Conceptualization. **Elisa Torresani:** Writing – review & editing, Software, Methodology, Conceptualization. **Eugene A. Olevsky:** Writing – review & editing, Validation, Supervision, Conceptualization.

Declaration of Competing Interest

The authors declare that they have no known competing financial interests or personal relationships that could have appeared to influence the work reported in this paper.

Acknowledgements

The support of Cerion Materials is gratefully appreciated. The support of US Army DEVCOM - Army Research Laboratory (Contract W911-NF-20–2–0226) is gratefully appreciated. The support of the National Science Foundation (Grants 2138421 and 2119832) is gratefully acknowledged. The support of the US Department of Energy, Office of Basic Energy Sciences (Award No. SC0022244) of the process modeling activities of SDSU researchers is gratefully appreciated.

Appendix A. Supporting information

Supplementary data associated with this article can be found in the online version at doi:10.1016/j.jeurceramsoc.2024.116700.

References

[1] F. Thévenot, Boron carbide—a comprehensive review, J. Eur. Ceram. Soc. 6 (1990) 205–225, https://doi.org/10.1016/0955-2219(90)90048-K.
[2] A.K. Suri, C. Subramanian, J.K. Sonber, T.S.C. Murthy, Synthesis and consolidation of boron carbide: a review, Int. Mater. Rev. 55 (2010) 4–40, https://doi.org/10.1179/095066009X12506721665211.
[3] V. Domnich, S. Reynaud, R.A. Haber, M. Chhowalla, Boron carbide: Structure, properties, and stability under stress, J. Am. Ceram. Soc. 94 (2011) 3605–3628, https://doi.org/10.1111/j.1551-2916.2011.04865.x.
[4] S.S. Rehman, W. Ji, Z. Fu, W. Wang, H. Wang, M. Asif, J. Zhang, In situ synthesis and sintering of B4C/ZrB2 composites from B4C and ZrH2 mixtures by spark plasma sintering, J. Eur. Ceram. Soc. 35 (2015) 1139–1145, https://doi.org/10.1016/j.jeurceramsoc.2014.10.013.
[5] D.V. Dudina, D.M. Hulbert, D. Jiang, C. Unuvar, S.J. Cytron, A.K. Mukherjee, In situ boron carbide-titanium diboride composites prepared by mechanical milling and subsequent Spark Plasma Sintering, J. Mater. Sci. 43 (2008) 3569–3576, https://doi.org/10.1007/s10853-008-2563-8.
[6] M. Saeedi Heydari, H.R. Baharvandi, Effect of different additives on the sintering ability and the properties of B4C-TiB2 composites, Int. J. Refract. Met. Hard Mater. 51 (2015) 61–69, https://doi.org/10.1016/j.ijrmhm.2015.02.014.
[7] P. Mogilevsky, E.Y. Gutmanas, I. Gotman, R. Telle, ChemInform abstract: reactive formation of coatings at boron carbide interface with Ti and Cr powders, ChemInform 26 (1995), https://doi.org/10.1002/chin.199541277.
[8] J.E. Zorzi, C.A. Perottoni, J.A.H. Da Jornada, Hardness and wear resistance of B4C ceramics prepared with several additives, Mater. Lett. 59 (2005) 2932–2935, https://doi.org/10.1016/j.matlet.2005.04.047.
[9] J. Zhang, F. Meng, R.I. Todd, Z. Fu, The nature of grain boundaries in alumina fabricated by fast sintering, Scr. Mater. 62 (2010) 658–661, https://doi.org/10.1016/j.scriptamat.2010.01.019.

[10] H.-W. Kim, Y.-H. Koh, H.-E. Kim, Densification and mechanical properties of B4C with Al2O3 as a sintering aid, J. Am. Ceram. Soc. 83 (2004) 2863–2865, https://doi.org/10.1111/j.1151-2916.2000.tb01647.x.
[11] E.A. Olevsky, C. Garcia-Cardona, W.L. Bradbury, C.D. Haines, D.G. Martin, D. Kapoor, Fundamental aspects of spark plasma sintering: II. Finite element analysis of scalability, J. Am. Ceram. Soc. 95 (2012) 2414–2422, https://doi.org/10.1111/j.1551-2916.2012.05096.x.
[12] E.A. Olevsky, D.V. Dudina, Field-Assisted Sintering, Springer International Publishing, Cham, 2018, https://doi.org/10.1007/978-3-319-76032-2.
[13] Z.A. Munir, U. Anselmi-Tamburini, M. Ohyanagi, The effect of electric field and pressure on the synthesis and consolidation of materials: a review of the spark plasma sintering method, J. Mater. Sci. 41 (2006) 763–777, https://doi.org/10.1007/s10853-006-6555-2.
[14] Z.A. Munir, D.V. Quach, M. Ohyanagi, Electric current activation of sintering: a review of the pulsed electric current sintering process, J. Am. Ceram. Soc. 94 (2011) 1–19, https://doi.org/10.1111/j.1551-2916.2010.04210.x.
[15] X. Li, D. Jiang, J. Zhang, Q. Lin, Z. Chen, Z. Huang, Densification behavior and related phenomena of spark plasma sintered boron carbide, Ceram. Int. 40 (2014) 4359–4366, https://doi.org/10.1016/j.ceramint.2013.08.106.
[16] S. Grasso, J. Poetschke, V. Richter, G. Maizza, Y. Sakka, M.J. Reece, Low-temperature spark plasma sintering of pure nano WC powder, J. Am. Ceram. Soc. 96 (2013) 1702–1705, https://doi.org/10.1111/jace.12365.
[17] X. Wei, C. Back, O. Izhvanov, O.L. Khasanov, C.D. Haines, E.A. Olevsky, Spark plasma sintering of commercial zirconium carbide powders: densification behavior and mechanical properties, Mater. (Basel) 8 (2015) 6043–6061, https://doi.org/10.3390/ma8095289.
[18] D. Lahiri, E. Khaleghi, S.R. Bakshi, W. Li, E.A. Olevsky, A. Agarwal, Graphene-induced strengthening in spark plasma sintered tantalum carbide-nanotube composite, Scr. Mater. 68 (2013) 285–288, https://doi.org/10.1016/j.scriptamat.2012.10.043.
[19] Y. Liu, S. Ge, Y. Huang, Z. Huang, D. Zhang, Influence of sintering process conditions on microstructural and mechanical properties of boron carbide ceramics synthesized by spark plasma sintering, Mater. (Basel) 14 (2021) 1–14, https://doi.org/10.3390/ma14051100.
[20] E.A. Olevsky, Theory of sintering: From discrete to continuum, Mater. Sci. Eng. R. Rep. 23 (1998) 41–100, https://doi.org/10.1016/S0927-796X(98)00009-6.
[21] C. Van Nguyen, S.K. Sistla, S. Van Kempen, N.A. Giang, A. Bezold, C. Broeckmann, F. Lange, A comparative study of different sintering models for Al2O3, J. Ceram. Soc. Jpn. 124 (2016) 301–312. ⟨https://www.jstage.jst.go.jp/article/jcersj2/124/4/124_15257/_article/-char/ja/⟩.
[22] C. Manière, C. Harnois, S. Marinel, Porous stage assessment of pressure assisted sintering modeling parameters: a ceramic identification method insensitive to final stage grain growth disturbance, Acta Mater. 211 (2021), https://doi.org/10.1016/j.actamat.2021.116899.
[23] B. Sarbandi, J. Besson, M. Boussuge, D. Ryckelynck, F. Barlat, Y.H. Moon, M.G. Lee, Anisotropic Const. Model FE Simul. Sinter. Process slip Cast. Tradit. Porcelain, (2010) 689–696, https://doi.org/10.1063/1.3457622.
[24] T. Kraft, H. Riedel, Numerical simulation of solid state sintering; model and application, J. Eur. Ceram. Soc. (2004), https://doi.org/10.1016/S0955-2219(03)00222-X.
[25] R.K. Bordia, R. Zuo, O. Guillon, S.M. Salamone, J. Rödel, Anisotropic constitutive laws for sintering bodies, Acta Mater. 54 (2006) 111–118, https://doi.org/10.1016/j.actamat.2005.08.025.
[26] O. Gillia, D. Bouvard, Phenomenological analysis of densification kinetics during sintering: application to WC-Co mixture, Mater. Sci. Eng. A. (2000), https://doi.org/10.1016/S0921-5093(99)00621-8.
[27] C. Manière, C. Harnois, S. Marinel, Role of microstructure reactivity and surface diffusion in explaining flash (ultra-rapid) sintering kinetics, J. Eur. Ceram. Soc. 43 (2023) 2057–2068, https://doi.org/10.1016/j.jeurceramsoc.2022.12.006.
[28] W. Li, E.A. Olevsky, J. McKittrick, A.L. Maximenko, R.M. German, Densification mechanisms of spark plasma sintering: multi-step pressure dilatometry, J. Mater. Sci. 47 (2012) 7036–7046, https://doi.org/10.1007/s10853-012-6515-y.
[29] G. Lee, C. Manière, J. McKittrick, E.A. Olevsky, Electric current effects in spark plasma sintering: From the evidence of physical phenomenon to constitutive equation formulation, Scr. Mater. 170 (2019) 90–94, https://doi.org/10.1016/j.scriptamat.2019.05.040.
[30] S.J. Park, P. Suri, E. Olevsky, R.M. German, Master sintering curve formulated from constitutive models, J. Am. Ceram. Soc. 92 (2009) 1410–1413, https://doi.org/10.1111/j.1551-2916.2009.02983.x.
[31] T. Grippi, S. Béhar-Lafenetre, H. Friedrich, D. Haas, U. Schenderlein, S. Marinel, C. Manière, Grain growth modeling for gas pressure sintering of silicon nitride based ceramics, Mater. Today Commun. 34 (2023), https://doi.org/10.1016/j.mtcomm.2022.105189.
[32] J. Diatta, E. Torresani, A. Maximenko, C. Haines, D. Martin, E. Olevsky, Peltier effect during spark plasma sintering of boron carbide, Results Phys. 29 (2021) 104719, https://doi.org/10.1016/j.rinp.2021.104719.
[33] M. Mashhadi, E. Taheri-Nassaj, V.M. Sglavo, Pressureless sintering of boron carbide, Ceram. Int. 36 (2010) 151–159, https://doi.org/10.1016/j.ceramint.2009.07.034.
[34] P.D. Williams, D.D. Hawn, Aqueous dispersion and slip casting of boron carbide powder: effect of pH and oxygen content, J. Am. Ceram. Soc. 74 (1991) 1614–1618, https://doi.org/10.1111/j.1151-2916.1991.tb07147.x.
[35] R.M. German, German, Sintering theory and practice, Chapitre. (1996).
[36] M. Demuynck, J.P. Erauw, O. Van der Biest, F. Delannay, F. Cambier, Densification of alumina by SPS and HP: A comparative study, J. Eur. Ceram. Soc. 32 (2012) 1957–1964, https://doi.org/10.1016/j.jeurceramsoc.2011.10.031.
[37] J.A. Wurst, J.C, Nelson, Lineal intercept method for measuring grain size in two-phase polycrystalline ceramics, J. Am. Ceram. Soc. 55 (1972) 109.
[38] V.V. Skorohod, Rheological basis of the theory of sintering, Nauk. Dumka, Kiev. (1972).
[39] M.S. Koval'chenko, Y.G. Tkachenko, L.F. Ochkas, D.Z. Yurchenko, V.B. Vinokurov, Theory and Technology of Sintering, Therm. Chem. Treat. Process. Densif. Kinet. Boron Carbide Hot Press. 25 (1987) 18–21.
[40] J. Wang, R. Raj, Estimate of the activation energies for boundary diffusion from rate-controlled sintering of pure alumina, and alumina doped with zirconia or titania, J. Am. Ceram. Soc. 73 (1990) 1172–1175, https://doi.org/10.1111/j.1151-2916.1990.tb05175.x.
[41] F. Raether, P. Schulze Horn, Investigation of sintering mechanisms of alumina using kinetic field and master sintering diagrams, J. Eur. Ceram. Soc. 29 (2009) 2225–2234, https://doi.org/10.1016/j.jeurceramsoc.2009.01.025.
[42] C. Manière, T. Grippi, S. Marinel, Estimate microstructure development from sintering shrinkage: a kinetic field approach, Mater. Today Commun. 31 (2022), https://doi.org/10.1016/j.mtcomm.2022.103269.
[43] T.G. Abzianidze, A.M. Eristavi, S.O. Shalamberidze, Strength and creep in boron carbide (B4C) and aluminum dodecaboride (αAlB12), J. Solid State Chem. 154 (2000) 191–193, https://doi.org/10.1006/jssc.2000.8834.
[44] C. Manière, J.S. Diatta, C. Couder, C. Harnois, S. Marinel, Spark plasma sintering grain growth assessment by densification kinetics analysis, Scr. Mater. 228 (2023), https://doi.org/10.1016/j.scriptamat.2023.115346.
[45] J. Diatta, G. Antou, N. Pradeilles, A. Maître, Numerical modeling of spark plasma sintering—Discussion on densification mechanism identification and generated porosity gradients, J. Eur. Ceram. Soc. 37 (2017) 4849–4860, https://doi.org/10.1016/j.jeurceramsoc.2017.06.052.
[46] C. Manière, L. Durand, E. Brisson, H. Desplats, P. Carré, P. Rogeon, C. Estournès, Contact resistances in spark plasma sintering: From in-situ and ex-situ determinations to an extended model for the scale up of the process, J. Eur. Ceram. Soc. 37 (2017) 1593–1605, https://doi.org/10.1016/j.jeurceramsoc.2016.12.010.
[47] C. Manière, G. Lee, E.A. Olevsky, Proportional integral derivative, modeling and ways of stabilization for the spark plasma sintering process, Results Phys. 7 (2017) 1494–1497, https://doi.org/10.1016/j.rinp.2017.04.020.
[48] M. Bouchacourt, F. Thevenot, The correlation between the thermoelectric properties and stoichiometry in the boron carbide phase B4C-B10.5C, J. Mater. Sci. 20 (1985) 1237–1247, https://doi.org/10.1007/BF01026319.
[49] G. With, High temperature fracture of boron carbide: experiments and simple theoretical models, J. Mater. Sci. 19 (1984) 457–466, https://doi.org/10.1007/bf00553569.
[50] X. Wei, D. Giuntini, A.L. Maximenko, C.D. Haines, E.A. Olevsky, Experimental investigation of electric contact resistance in spark plasma sintering tooling setup, J. Am. Ceram. Soc. 98 (2015) 3553–3560, https://doi.org/10.1111/jace.13621.